ChemElectroChem

Research Article
doi.org/10.1002/celc.202400080

Chemistry Europe
European Chemical Societies Publishing

www.chemelectrochem.org

Electrochemical Behaviour and Sensing of Chlorpromazine at Polymer-Free Kaolin-Based Nanosodalite and Nanosodalite-Graphene Foam Film modified Glassy Carbon Electrodes

Firmin Parfait Tchoumi,[a, b] Cyrille Ghislain Fotsop,[c] Guy Bertrand Tamne,[d] Henrietta W. Langmi,[e] Justin Claude Kemmegne-Mbouguen,*[a] and Emmanuel Ngameni[b]

A nanosodalite (SOD) was synthesized utilizing Cameroonian kaolin and then used to prepare a nanocomposite (SOD-GF) with graphene foam (GF). The as-synthesized materials were characterized using X-ray diffractometry (XRD), Fourier transform-infrared (FT-IR) spectroscopy, N_2 adsorption-desorption and scanning electron microscopy coupled with emission dispersive X-ray (SEM/EDX). The results show a pure sodalite with high degree of crystallinity with crystallite size and BET surface area of 38.3 nm and 22 m^2/g, respectively. The composite's characterization revealed a well-integrated material in which the structural integrity of each material is maintained, its surface area being 4-fold that of pristine SOD. Stable SOD and SOD-GF modified glassy carbon electrode (GCE) were prepared by drop coating without a binder and utilized to study the electrochemistry of chlorpromazine (CPZ) in acidic, neutral and basic pHs. It appeared that (i) CPZ's electrochemical oxidation was a two-step one-electron process at SOD/GCE and a one-step two-electron process at SOD-GF/GCE and (ii) the electrochemical reaction mechanism was an EEC mechanism at SOD/GCE while at SOD-GF/GCE the mechanism was EEC at pH $<$ 4 and EC for greater pH. SOD/GCE and SOD-GF/GCE were used to sense CPZ within CPZ's concentration ranging from 0.5-30 μM with low detection limits.

Introduction

Chemically modified electrodes are continuously attracting researchers in the domain of electrochemical sensors, the challenge being to have direct control over the chemical nature of the electrode[1] which leads to enhanced sensitivity and selectivity over unmodified electrodes. During the past decades a wide range of research have been focused on the use of different materials for the electrode surface modification and their use as sensors, biosensors and immunosensors.[2] These materials include for example, aluminosilicates (clays and zeolites) and their composites (metal-organic framework/clay,[3] zeolite/acetylene black carbon.[4] Among these materials, zeolite materials occupy a prominent place due to their high cation exchange capacity and their well-defined rigid structure consisting of cages and channels which can affect the electron transfer reactions at electrode-zeolite-solution interface.

Sodalite zeolite is a traditional zeolite with a cubic framework having only β-cages (sodalite cages) composed of eight 6-membered and six 4-membered rings of alternating SiO_4 and AlO_4 tetrahedra.[5] It is characterized by the highest thermodynamic stability among all zeolites,[6] high ion exchange capacity and small pore size (0.28 nm[7]), which makes it a suitable material in selective separation[8] and for hydrogen storage.[9] Sodalites are synthesized as other zeolites using an alumina source and a silica source via different methods, which generally require long crystallization time,[10] high temperature[10b,11] and organic additives.[7,10a] Kaolin has appeared to be an ideal natural source of silica and alumina for efficient eco-friendly synthesis of zeolite[12] although it still needs organic structure directing agent, high temperature and long crystallization time.[13] Compared to the other reported methods of zeolite synthesis, solid-solid transformation has emerged as a simple and efficient method for the nanozeolite synthesis since it shortens nucleation and crystal growth and reduces elemental losses.[14] Contrary to other zeolites exhibiting large pores and high surface areas making them suitable for modification of the electrode for analytical purposes,[15] the aforementioned small pore size and low specific surface area of

[a] F. Parfait Tchoumi, J. Claude Kemmegne-Mbouguen
Laboratory of Nanomaterial for Sensors and Energy, Faculty of Science, University of Yaounde 1, P. O. Box 812 Yaounde, Cameroon
E-mail: jkemmeg@yahoo.fr
justin.kemmegne@facsciences-uy1.cm

[b] F. Parfait Tchoumi, E. Ngameni
Laboratoire d'Electrochimie et de Génie des Matériaux, Faculté des Sciences, Université de Yaoundé Ab B.P. 812 Yaoundé, Cameroun

[c] C. Ghislain Fotsop
Otto-von-guericke-University Magdeburg, Chemical Institute Industrial Chemistry, Universitâtsplatz 2, 39106 Magdeburg, Germany

[d] G. Bertrand Tamne
Department of Chemistry, High Teacher Training College, University of Yaounde 1, P. O. Box 49 Yaounde, Cameroon

[e] H. W. Langmi
Department of Chemistry, University of Pretoria, Private Bag, X20,Pretoria, Hatfield, 0028, South Africa

Supporting information for this article is available on the WWW under https://doi.org/10.1002/celc.202400080

sodalite together with poor conductivity limit its application in the field of electrochemistry. This limitation exists despite the large external surface with more silanol (Si–OH) and aluminol (Al-OH) groups likely to affect the electron transfer property.[16] To overcome these challenges sodalite-based composites consisting of sodalite doped with metal, have been employed for the chemical modification of the electrode substrate for the electrocatalytic oxidation of alcohols[17] and the quantification of some compounds of biological interest.[18]

Antipsychotic drugs are nowadays highly needed because they are utilized for the treatment of growing health problems due to psychological stress, anxiety and emotional disorder. Chlorpromazine (CPZ) is the first generation of drug widely used for this family. It is a drug of the phenothiazine family derivative acting as an antagonist of neurotransmitters such as dopamine.[19] CPZ is a representative and important member of tranquilizing agent including for promazine, trifluoperazine, and triflupromazine. Its overdose (>200 mg/day for oral administration and >50 mg for intramuscular injection[20]) was reported to cause high risk for baby and women during breast feeding.[20] In addition, CPZ is an emergent pollutant[21] since its prolonged consumption (several months) led to high urinary excretion of the consumers[22] and thus justifying its presence in ground water. Hence many techniques including high performance liquid chromatography,[21] capillary gas chromatography[23] and spectrofluorometric[24] have been successfully employed in the detection and quantification of CPZ as well as its degradation monitoring in drug and biological fluids. Recently, electrochemical techniques have shown to be accurate and faster, and they do not require arduous sample preparation for the detection of CPZ, using biomembrane[25][26]and chemically modified electrodes[27][28]with improved sensitivity compared to conventional electrodes.

In the present work we report the preparation of nanosized sodalite (SOD) zeolite using natural Cameroonian quartz-rich kaolin, and nanocomposite sodalite-graphene foam (SOD-GF), the latter material was obtained by combining the zeolite with graphene foam. Taking advantage of the nanosize of the as-synthesized sodalite, and the unique electronic property and large pores of graphene foam, glassy carbon electrode (GCE) modified with a stable film of either SOD or SOD-GF without a binder was utilized to assess the electrochemical behavior of CPZ and its sensitive detection in aqueous media. The nanocomposite modified electrode was also successfully used to quantify CPZ in a pharmaceutical tablet and in tap water.

Experimental Section

Materials, Chemicals and Reagents

The nanosodalite (SOD) used in this work was synthesized using beneficiated rich quartz content kaolin (BK) as silica and alumina source as previously reported,[29] the natural kaolin being sampled in the Mayouom's deposits in the western part of Cameroon. The beneficiation of the raw clay was achieved by the extraction of fine fraction of natural kaolin in order to significantly decrease the quartz content in raw kaolin. The chemical analysis of the beneficiated clay obtained reveals a low amount of quartz (6%) and increased kaolinite content (80%) compared to the raw kaolin (RK) as reported in our previous work.[29]

The graphene foam shortened as GF was obtained by chemical vapour deposition (CVD) as reported previously.[30] The chemicals utilised in this work were analytical grade reagent and were used as received. $K_3Fe(CN)_6$ (>99%), $[Ru(NH_3)_6Cl_3$ (98%), KCl (99%), N,N-dimethylmethanamide (DMF, 99,8%), and chlorpromazine (CPZ, 99%), were acquired from Abcr. Phosphoric acid (85%), boric acid (99.99%) and acetic acid (99%), were from Sigma-Aldrich. The solution of Britton-Robinson buffer (BR) with pH ranging from 3 to 10 was prepared using a mixture of H_3BO_3, H_3PO_4 and CH_3COOH in deionised water. The pH of the buffer was adjusted to the desired pH using NaOH solution (0.2 M)

Preparation of Nanosodalite, Graphene Foam and Sodalite-Graphene Foam Composite

The nanosodalite was synthesized using solid-solid transformation method as described by Choy et al.[31] The metakaolinite (BMk) used in this synthesis was obtained by calcining the treated kaolin (BK) for 2 hours at 600 °C. The alkaline clay solid gel was then prepared by hand mixing 1 g of BMk with 5 g of solid NaOH. Then, 1 mL of distilled water was added to the solid gel and mixed again in order to obtain a homogeneous paste with molar ratio of 1.67 SiO_2:Al_2O_3:13.41 Na_2O:0.01 H_2O. The resulting paste was thermally treated for 2 hours at 100 °C under static condition. The solid collected was washed with distilled water until the pH of the filtrate reached 8 and then dried for 12 h at 110 °C

The graphene foam was prepared as reported previously.[30] Briefly, nickel foam was heated under argon flow from 5 °C to 800 °C in a tubular furnace. It was then annealed for 20 min at 800 °C under argon/hydrogen flow, after which the temperature was ramped to 1000 °C at 5 °C/min. Acetylene used as the carbon source was then added and left for 15 min at 1000 °C. This was followed by cooling of the furnace to room temperature. The sample was removed from the furnace, coated with polymethyl methacrylate solution, calcined at 180 °C and soaked in hydrocholoric acid at 80 °C in order to etch nickel from the sample. Finally, the sample was pyrolyzed for 15 min at 800 °C to remove the polymethyl methacrylate, washed and air dried to obtain GF.

The sodalite-graphene foam composite namely SOD-GF was prepared by mixing GF with SOD powder in the presence of N,N-dimethylformamide (DMF). This consisted of dispersing separately 2-x mg of SOD in 0.5 mL of DMF and x mg of graphene in another 0.5 mL of DMF (where $x=0$, 0.05, 0.1, 0.2, 0.4, 0.5 or 0.6), then the first suspension was added to the second one under stirring at room temperature. The obtained suspension was sonicated for 30 min to have a well homogeneous suspension and kept again under stirring at room temperature for 24 h.

Instrumentation

The crystalline structure of SOD, GF and the composite were analysed using Powder X-ray diffraction (pXRD) performed on Rigaku Ultima IV X-ray diffractometer with CBO technology using Ni-filtered CuKα radiation (wavelength = 0.154 nm). The zeta potential (ZP) measurement was performed using a zetasizer (Brookhaven instruments, Co., USA). 2 mg of powder was introduced in 3 mL of deionised water and the pH of the suspension was adjusted from 2 to 12 using either NaOH (0.1 M) or HCl solution. The isoelectric point (IEP) was determined by plotting the obtained ZP versus pH of the solution.

The materials images were obtained using Auriga cobra Focused-Ion Beam scanning electron Microscope (FIB-SEM). The elemental composition was determine using Energy-dispersive X-ray (EDX) analysis performed on Field-emission scanning electron microscopy equipped with EDX spectroscopy. FTIR spectra recorded in the region 400–4500 cm^{-1} on Alpha IR spectrometer from Bruker was used to identify functional groups. The porosity characteristics of SOD and SOD-GF were obtained by N_2 sorption measurement at 77 K using Micromeritics ASAP 2020 HD instrument. Their particle size distribution was measured by dynamic light scattering (DLS) utilizing a Malvern Zetasizer Nano-(Malvern Instruments) at 25 °C. All Electrochemical measurements were conducted in a conventional three electrodes (Ag/AgCl as reference electrode, Platinum wire as counter electrode and bare and modified glassy carbon as working electrode) cell assembly on CorrTest potentiostat/galvanostat instrument equipped with CS studio5 electrochemical analysis system.

Preparation of the SOD/GCE and SOD-GF/GCE

The glassy carbon film electrodes were prepared by drop coating of 10 μL of either SOD or SOD-GF suspension prepared in DMF solvent (2 g/L) and then allowed to dry at room temperature for 1 h. Before the electrode modification, the bare substrate was first polished separately to a mirror like surface using aqueous alumina slurry obtained using three different grain sizes (1, 0.3, 0.05 μm) on wet polishing cloths. The modified electrodes were denoted SOD/GCE when pristine sodalite suspension was dropped and SOD-GF/GCE when the composite was employed.

Chlorpromazine Real Samples Preparation

A pharmaceutical tablet purchased in a local pharmacy containing chlorpromazine, labeled *Largactil* (100 mg, SANOFI), and tap water containing CPZ were used as two CPZ real samples for the determination of their CPZ contents. The tablet was finely ground in a mortar with a pestle, an adequate amount required for appropriate concentration was separately transferred into a 100 mL volumetric flask and dissolved with RB pH 7.12. The contents of the flask were sonicated for 5 min to complete dissolution, then centrifuged and filtered. For tap water sample, a known amount of CPZ was spiked in tap water (pH: 5.86; conductivity 94 μS/cm) without purification.

Results and Discussion

Physicochemical Characterization of SOD and SOD-GF

Structural and Morphological Studies

Figure 1A exhibits the XRD pattern of beneficiated clay, BK (pattern a), calcined beneficiated clay, BMk (pattern b), sodalite, SOD (pattern c) and sodalite-graphene composite, SOD-GF (pattern d). The diffractogram (a) of BK exhibits characteristic kaolinite peaks at 12.26°, 19.93°, and 24.53° in addition to the 2θ peaks of quartz at 20.72° and 26.53°. As expected, the disappearance of characteristic 2θ peaks of kaolinite was observed on the pattern (b) of the product of the calcination of the pristine clay. This is due to the dehydroxylation of kaolinite to obtained metakaolinite (BMk). After 2 h of thermal treatment of BMk the diffractogram (c) of the obtained material displayed the main characteristic peaks of sodalite at 14.07°, 19.98°, 24.57°, 28.43°, 31.88°, 35.07°, 38.01° and 43.18°[32] with good crystallinity (96%). Interestingly, the disappearance of the characteristic quartz peaks in the diffractogram of the sodalite is noted, which is contrary to what was reported by Choy et al[31] and Song et al.[33] These results confirm that (i) the synthesized sodalite was pure, (ii) the solid-solid transformation performed on fine fraction of BMk facilitated the rapid dissolution of silicon and aluminum species through a short range molecular rearrangement.[31] From the XRD data and by using Sherrer's equation (Eq.1), the relative crystallinity was calculated according to Eq. 1[34] below:

$$\%\ \text{Crystallinity} = \frac{\text{Area of crystalline peaks}}{\text{Area of all peaks (crystalline + amorphous)}} x100 \quad (1)$$

The Scherrer equation $d = \frac{K\lambda}{\beta cos\theta}$ (Eq. 2) was utilized to estimate the average crystallite size (d in nm) of the composite material in this equation, K is the Scherrer constant equal to 0.9, λ (nm) the wavelength of the X-rays, θ the value of Bragg's angle of the most intense peak -(radian) and β is the full width at half-maximum (FWHM). The average crystallite size of the synthesized sodalite was estimated and was found to be 38.29 nm, indicating the nanoscale size of SOD. This crystallite size is close to that of the composite (ca 33.49 nm) suggesting that the size of the sodalite crystal was not influenced by the presence of graphene foam.

The FTIR spectra of the absorption bands of SOD (c) and its precursors BK (a) and BMk (b) are shown in Figure 1B. It is revealed clearly that the thermal activation of BK led to the disappearance of characteristic absorption bands of kaolinite (3692, 3658, 3667, 3620 cm^{-1}) confirming the formation of the metakaolinite used further for the synthesis of SOD. The spectrum (c) shows sodalite absorption bands, specifically, the bands at 718, 702 and 658 cm^{-1} characteristic bands of hydroxysodalite, in addition to the bands at 423 and 457 cm^{-1} related to the bending vibrations of T–O–T (T=Si or Al) bond as reported in the literature.[35] The single six-membered ring known as secondary building unit of hydroxyl sodalite is also highlighted by the weak band at *ca* 566 cm^{-1} as reported by Alkan et al[36] and Flanigen et al.[35] Moreover, the absorption bands at 950 cm^{-1} ascribed to the asymmetric Si–O–Al stretching vibration in zeolitic materials[37] is clearly observed. The broad band at 3300 cm^{-1} and the band at 1655 cm^{-1} are attributed to the zeolitic water. The FTIR spectrum together with the XRD pattern demonstrate the effectiveness of the synthesis of sodalite using BMk as starting material.

The EDX analysis of the as-synthesized nanosodalite (Figure S1) revealed that the elemental composition of SOD is mainly Si (11.9%), Al (12.9%) and Na (13.8%) and O (58.6%).

The SOD particle size was estimated using DLS analysis and the results presented in Figure 1E show the particle size distribution of the sodalite. It was found that the particle size of the nanosodalite's particle size ranges between 150 and 420 nm with a maximum at 297 nm. This value is quite different from the crystal size suggesting a polycrystalline character of

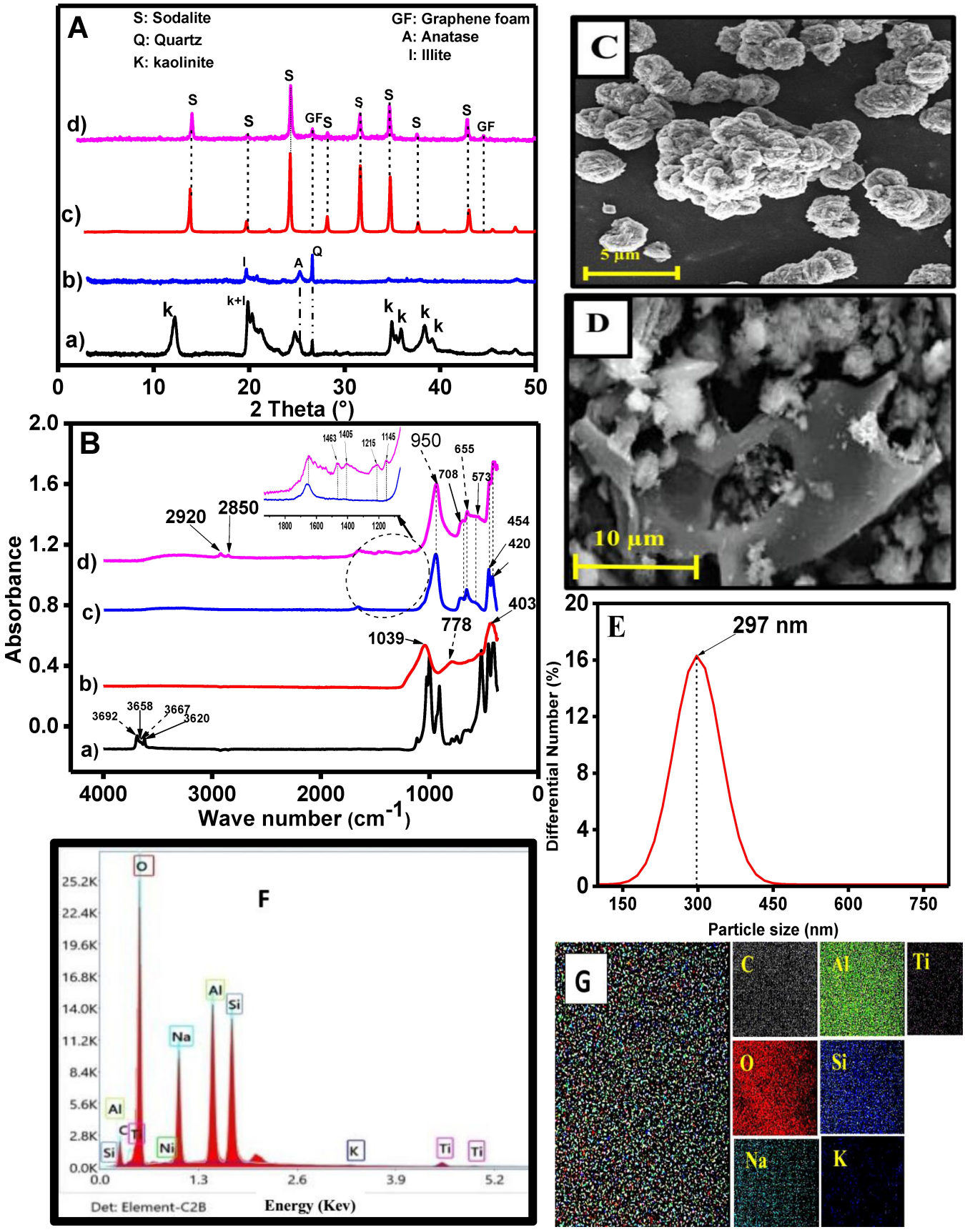

Figure 1. A) XRD pattern of a) BK, b) BMK, c) SOD and d) SOD-GF; **B**) FTIR of a) BK, b) BMK, c) SOD and d) SOD-GF; **C**) and **D**) SEM images of SOD and SOD-GF respectively; **E**) DLS spectrum of SOD; F) EDX spectrum of SOD-GF and **G**) EDX-mapping of SOD-GF

nanosodalite[14a,38] consistent with the crystallites aggregates as observed in SEM images (Figure 1C).

The composite SOD-GF was also characterized by XRD, FTIR and EDX. The diffractogram (d) in Figure 1A presents the XRD pattern of SOD-GF with 2θ peaks well aligned with characteristic 2θ peaks of sodalite, except additional peaks appearing at 26.5° and 44.6° attributed to the graphitic foam.[30] The intensities of the sodalite peaks were found to be lower than those of pristine SOD, suggesting a decrease in the crystallinity, probably because the SOD particles within the composite are located in the large graphene foam pore (see SEM image in Fig 1D) creating a heterogeneous structure,[39] the zeolitic framework of the embedded sodalite being retained. In Figure 1B, the IR spectrum (d) of the resulting composite presents absorption bands which are well aligned with those of SOD presented in spectrum (c) in addition to the characteristic bands of GF at 2920–2850 cm^{-1}, 1463 cm^{-1} and 1630 cm^{-1}, absent on spectrum d of pristine SOD. These new bands at 2920–2850 cm^{-1} and 1463 cm^{-1}, were assigned to the stretching vibration of C–H of methylene group[39–40] and the broad band at 1630 cm^{-1} was attributed to the skeletal vibrations of unoxidized C=C bonds of the graphitic domains associated with the stretching deformation of –OH of interlayer water.[39–40] Interestingly the bands at 1150 cm^{-1} and 1216 cm^{-1} corresponding to C–O bond is present on spectrum of the composite.[41] These results show within the composite SOD likely interacts with GF through van der Waals interaction involving the silanol and/or aluminol groups of SOD and C–H and C=C of GF.[42] The value of the crystallite size of the composite was found to be 33.49 nm which is close to that of the pristine sodalite

The results of the EDX analysis of the composite is exhibited in Figure 1F. It shows that its chemical composition (gathered in Table 1) was identical to that of the pristine SOD in addition to carbon (C) (*ca* 10.2%). Furthermore, Figure 1G shows the elemental mapping of the composite wherein the expected elements present in sodalite and carbon from GF were homogeneously distributed in the composite.

Textural Properties, Surface Charge and Thermal Behaviour Studies

The nitrogen adsorption/desorption isotherms of the nanosodalite (curve a) and the composite (curve b) are exhibited in Figure S2A. As shown by curve a) of this figure, almost no nitrogen was adsorbed by the nanosodalite at low pressures due to the small pore size of the sodalite preventing N_2 molecules to penetrate the zeolite. The BET surface area of the as-synthesized sodalite was estimated to be 22.02 m^2/g with total pore volume equal to 0.08 cm^3/g, in which the largest contribution to the latter is from the external surface area of the sodalite.[13] These values was found to be higher than those of the reported sodalite material obtained using kaolin as starting material.[13,43] This demonstrates the efficiency of beneficiated kaolin in the synthesis of high surface area nanozeolite[29] ascribed to the reported solid state reaction as a successful method to form nanocrystal sodalite.[38] Interestingly, the nitrogen was found to be adsorbed even at low pressure for the composite as shown by curve b, suggesting a more accessible composite exhibiting an average pore size of 0.95 nm and BET surface area of 83 m^2/g. These textural property values are four times higher than those of sodalite. This enhancement in textural properties of the composite is likely due to the presence of porous graphene foam, wherein the sodalite particles were incorporated.

Table 1. Elemental composition (atomic %) of SOD and SOD/GF

	Si	Al	O	Na	C	Ti	K
SOD	11.9	12.9	58.6	13.8	/	2.6	0.2
SOD/GF	9.6	10.6	55.9	13.4	10.2	0.2	0.1

The zeta potential values of SOD and SOD-GF were recorded as a function of pH of the solution, thus enabling the determination of their IEP as displayed in Figure S2 B. It can be observed for both SOD and SOD-GF that the zeta potential decreases while the pH of the solution increases. The zero zeta potential is obtained at pH 6.25 and 5.55, indicating that the IEP of SOD is 6.25 and that of SOD-GF is 5.55. The IEP of SOD is quite similar to that reported elsewhere.[44] Indeed zeolite materials are known to be structurally negatively charged regardless of the pH, thus the changes of the surface charge observed could be due to the adsorption of H^+ leading to the protonation of the silanol/aluminol groups (–Si(Al)-OH) of the zeolite to form -Si(Al)OH_2^+ in acidic media and their subsequent deprotonation in basic solution to form -Si-O^--Al.[45] For SOD-GF, the decrease of IEP to 5.55 is likely explained by the negatively charged surface of the graphene foam[46] structure which reduces the overall charge of the composite.

The TGA analysis was used to study the thermal behaviour of the synthesized pristine sodalite and the composite, and their thermogravimetric curves obtained are shown in Figures S2 C and S2 D, respectively. The TG curve of the sodalite shows an overall weight loss of *ca* 2.12% in three thermal events (see DTG curve): (i) the first loss of 1% centred at 100 °C corresponding to the loss of free or water physically adsorbed,[47] (ii) the second one of 1% at 228 °C attributed to the loss of water from hydration complexes formed with exchangeable cation[47] and (iii) the third slight loss of 0.12% at 436 °C resulting in the dehydroxylation proceeds by the destruction of hydroxyl bonds generated when exchangeable cation polarize water molecules[48] which is accompanied by a reorganization of a non-framework constituent.[49] The only exothermic peak observed on the heat flow curve at 902 °C indicates that the as-synthesized SOD is stable up to 902 °C and then decomposes to nepheline at higher temperatures.[49] Interestingly, the examination of TG curve of the composite (see Figure S2 D) reveals the loss of adsorbed water (6% and 5% weight at 70 °C and 186 °C, respectively). These losses are more significant than that of pristine SOD, probably because the porosity of the graphene foam within the composite has allowed the improvement of water absorption capacity in the different cavities. The weight loss of 5% between 200–600 °C is

attributed to the decomposition of organic material, meanwhile the significant weight loss of 8% centered at 679 °C is related to the carbon oxidation to carbon dioxide (CO_2).[30]

Electrochemical Characterization of SOD and SOD-GF Film Modified GCE

The ability of the pristine sodalite and the sodalite-graphene foam composite to form a stable thin film on GCE without a binder and its permeation properties toward redox anionic ($[Fe(CN)_6]^{3-}$) and cationic ($[Ru(NH_3)_6]^{3+}$) probe was studied using cyclic voltammetry (CV). Figure 2 shows the multisweep cyclic voltammograms recorded in diluted $[Fe(CN)_6]^{3-}$ (Figure 2A) or $Ru(NH_3)_6]^{3+}$ in 0.1 M KCl (Figure 2B) at bare GCE (CV a) and GCE coated with either SOD (SOD/GCE (CV b)) or SOD-GF (SOD-GF/GCE (CV c)). The CV recorded in diluted $[Fe(CN)_6]^{3-}$ (0.5 mM) at SOD/GCE shows no noticeable peak, suggesting that as aluminosilicate film GCE, SOD behaves as a barrier for the negatively charged redox probe to access GCE surface where it will react. At sodalite/graphene foam composite film GCE, the recorded CV exhibits a quasi-reversible process (Ipa = 2.15 μA, Ipc = 2.50 μA) with the peak to peak △E = 370 mV, while at unmodified GCE, the recorded CV presents a well resolved peak centered at + 200 mV with △E = 130 mV and current ratio Ipa/Ipc ≈ 1. These results indicated the presence of graphene foam within the film favoured the diffusion of the negative probe to the carbon surface or its transfer capability, and facilitates the redox reaction of the probe. When the anionic probe was replaced by the cationic one, the multisweep of the potential at SOD-GF/GCE led to gradual increase of redox peak current which stabilized after 20 scans (Fig 3B), thereby indicating the preconcentration capability of the composite. In the same conditions at bare GCE or SOD modified GCE, the recorded CVs shows well-defined redox peaks with constant current peak (Ipa = 10.55 μA and Ipc = 12.75 μA for the both electrodes) upon repetitive scan potential, the maximum steady state current value obtained is half that recorded at SOD-GF/GCE. This result confirms the known affinity of negatively charged aluminosilicate for cationic species, and on the other hand the absence of accumulation of the cationic probe at SOD film GCE because of the low porosity of the material. Therefore, an extrazeolite mechanism is suggested for $[Ru(NH_3)_6]^{3+}$ at SOD/GCE. These finding indicates that the synergy effect of the electrical conducting mesoporous GF and the anionic nanozeolite favored the intake of the cationic species.

The electrochemical impedance spectroscopy (EIS) was used to study the charge transfer capability of the modified electrode. The Nyquist plots recorded in 0.1 M KCl containing $[Fe(CN)_6]^{3-/4-}$ (0.5 mM) at modified and unmodified electrode are presented in Figure 2C. From these plots, the charge transfer resistance (Rtc) corresponding to the diameter of the semi-circle of the Nyquist curve were estimated and were found to be respectively, 7.5 KΩ, 450 KΩ and 37.5 KΩ for bare GCE (plot a), SOD-GCE (plot c) and SOD-GF/GCE (plot b), indicating that SOD film displays a high resistance toward $[Fe(CN)_6]^{3-/4-}$ to access the surface of glassy carbon electrode surface. These results indicate that the presence of GF, owing to its electrical conductivity property increases the capability of the charge transfer and the diffusion properties of the SOD/GF composite onto the electrode surface, in good agreement with the cyclic voltammetry result.

Electrochemical Study of Chlorpromazine at SOD/GCE and SOD-GF/GCE

Zhang et al. reported that chlorpromazine oxidation followed an EEC in acidic pH and an EC mechanism in neutral pH involving two separate one-electron steps and one step two-electron oxidation, respectively.[50] Scheme 1 below presents the electrochemical mechanism and pathway of CPZ as reported in literature.[27b,50] Thus, before applying the modified electrodes (SOD/GCE and SOD-GF/GCE) to the detection and quantification of CPZ, its electrochemical behaviour was studied in acidic, neutral and basic pHs using BR buffer (BR) with appropriate pH.

Figure 3 shows the cyclic voltammograms recorded in 0.04 M BR buffer solution (pH 3 in Figure 3A, pH 7.12 in Figure 3B and pH 8.6 in Figure 3C) containing CPZ using bare GCE (CV (a)), SOD-GCE (CV (b)) and SOD-GF/GCE (CV (c)).

In acidic buffer (pH 3), when the potential is scanned at 50 mVs^{-1} in the positive direction (from 0 to + 1.2 V), two oxidation peaks namely A1 and A2 appeared on the voltammograms recorded at bare and modified electrodes. On the reverse scan only one reduction peak (C1) was observed. In addition, when the scan was recorded from less positive potential (+ 0.8 V) than the oxidation peak A2, the reduction peak C1 is always observed at about the same potential as the reduction peak recorded when the scanning potential was run in large potential window (0 to + 1.2 V). The reversible process corresponds to the one-electron oxidation of CPZ to $CPZ^{\cdot+}$ and the irreversible process to the one-electron oxidation of $CPZ^{\cdot+}$ to $CPZ^{2.+}$ as shown in scheme 1. This result indicates that the electrochemical mechanism oxidation of CPZ in this pH at modified and unmodified GCE is likely an EEC mechanism, the first redox process (A1, C1) being reversible (path I in scheme 1) and the second one being irreversible (path III in scheme 1). This behaviour is kept unchanged at pH 4, 5, and 6 at SOD/GCE contrary to the electrochemical behaviour observed at SOD-GF/GCE, where the oxidation peak A2 was not detectable, the process (A1, C1) remaining reversible (see Figure S3). This behaviour could be explained by the fact that the positively charged radical CPZ formed in the forward scan through one-electron transfer process is very stable in acidic media, and may exhibit favourable electrostatic interaction with the negatively charged zeolite, and thus allowing its diffusion to carbon surface where it can be partially oxidised to $CPZ^{2.+}$ and reduced to CPZ. In addition, the oxidation potential peak A1 at both modified electrode displayed a nearly constant value with a non-Nernstian slope of the plot Ep versus pH (see Figure 4A-a for SOD/GCE and Figure 4B-a for SOD-GF/GCE). This result suggests that the electrochemical process at both modified electrodes is pH independent, in agreement with other works reported in the literature.[51]

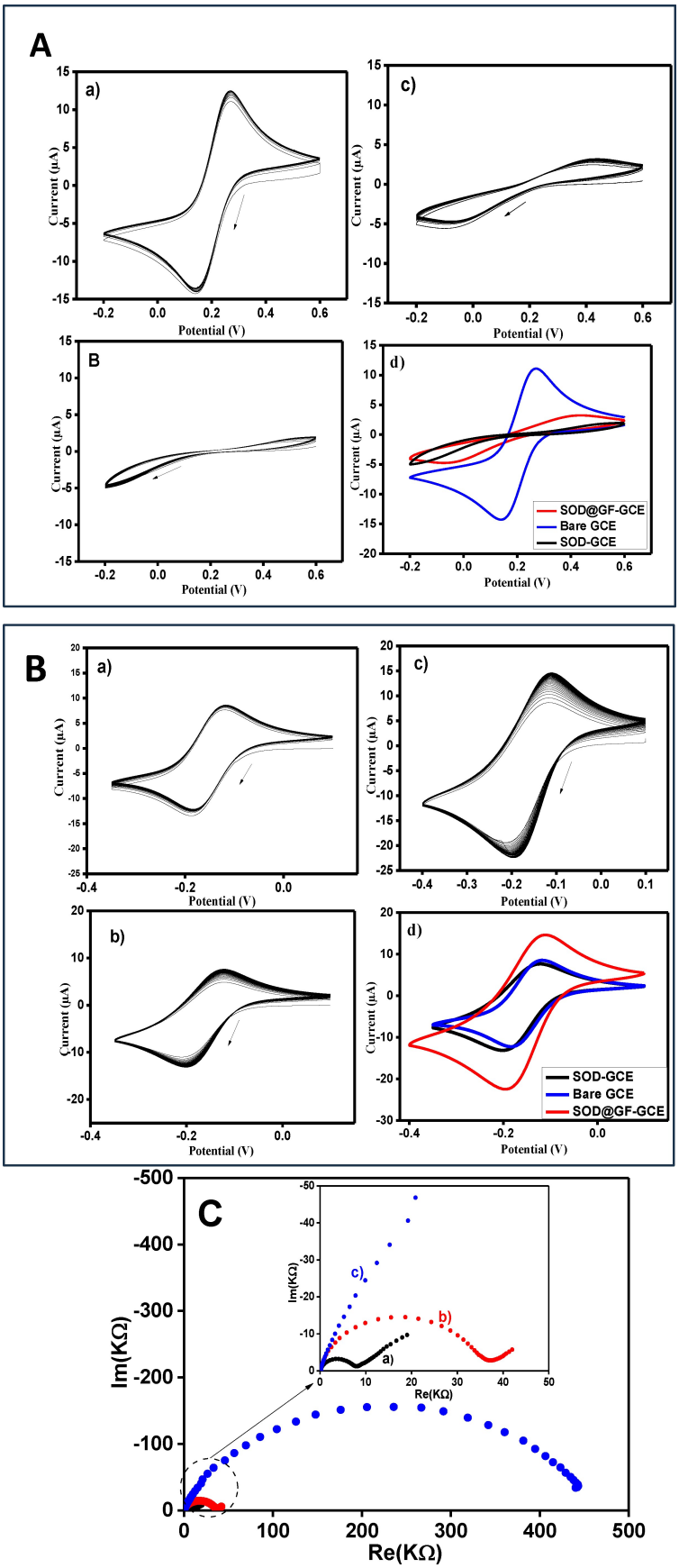

Figure 2. Multisweep cyclic voltammograms recorded in 0.1 M KCl containing **A**) 0.5 mM of $Fe(CN)_6^{3-}$ and **B**) $[Ru(NH_3)_6]^{3+}$ at: **a)** Bare GCE, **b)** SOD-GCE and **c**) SOD-GF/GCE at scan rate: 50 $mV.s^{-1}$; **d**) Superposition of cyclic voltammograms at equilibrium. **C)** Nyquist plots recorded onto a) bare GCE, b) SOD-GCE and c) SOD-GF-GCE in 0.1 M KCl in presence of 0.5 mM $Fe(CN)_6^{3-}/Fe(CN)_6^{4-}$

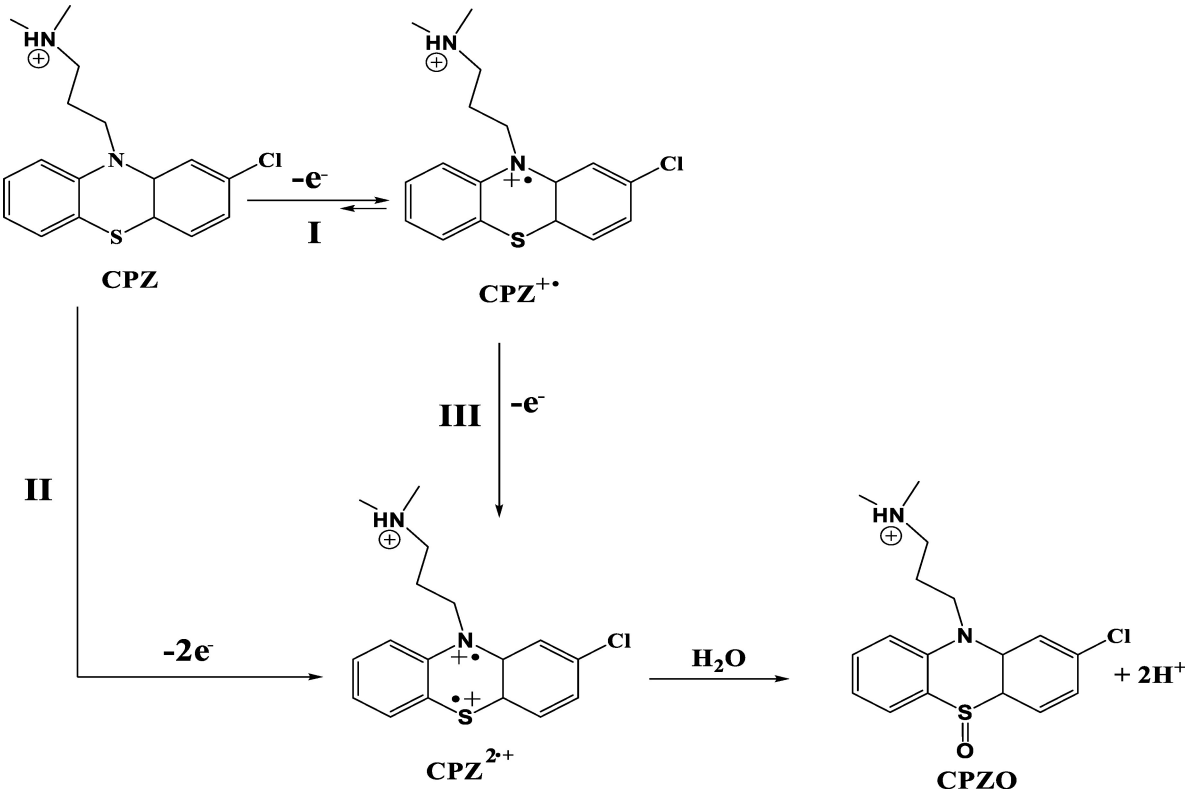

Scheme 1. Electrochemical reaction mechanism of CPZ[50–51]

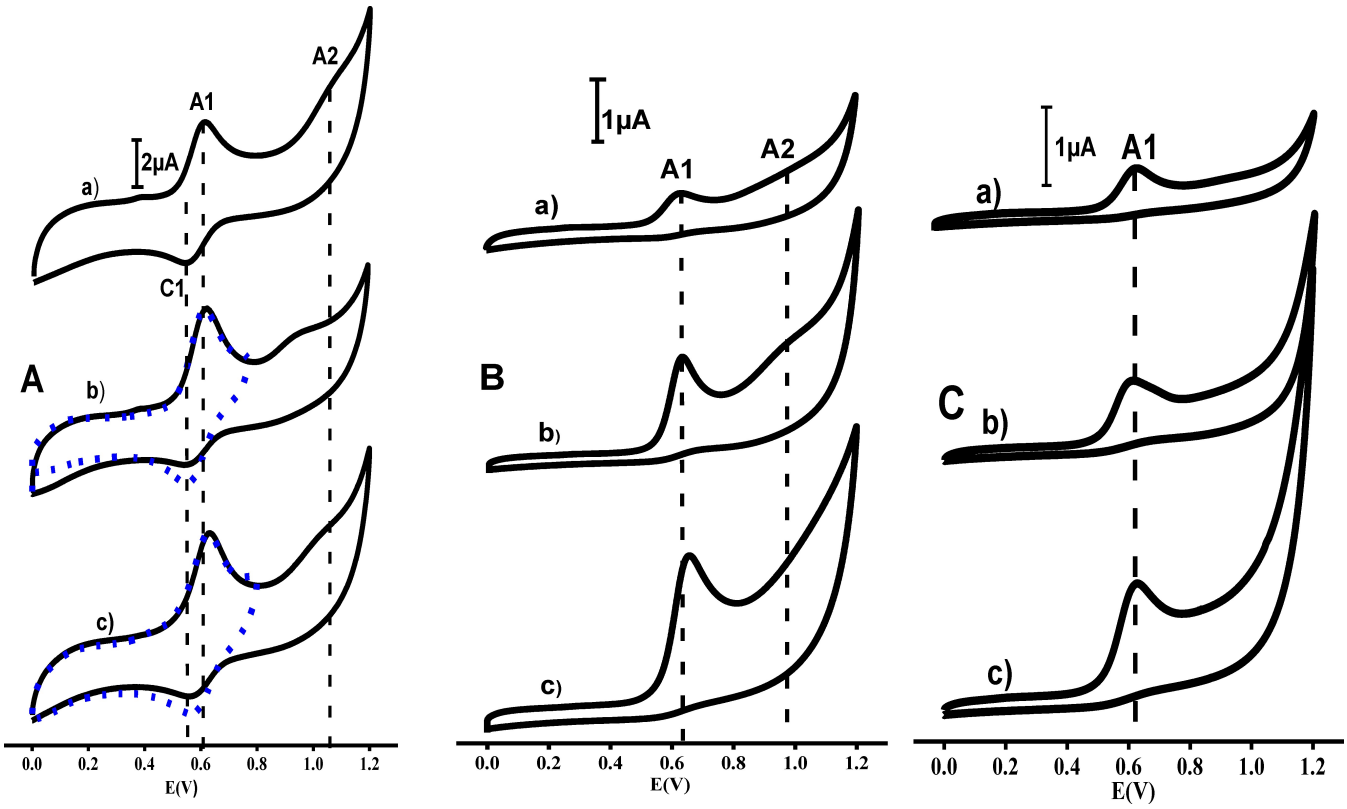

Figure 3. CVs recorded at 50 mV/s containing 29.5 μM of CPZ in **A)** RB pH 3, B) RB pH 7.12 and C) RB pH 8.6 at bare GCE (a), SOD/GCE (b) and SOD-GF/GCE (c).

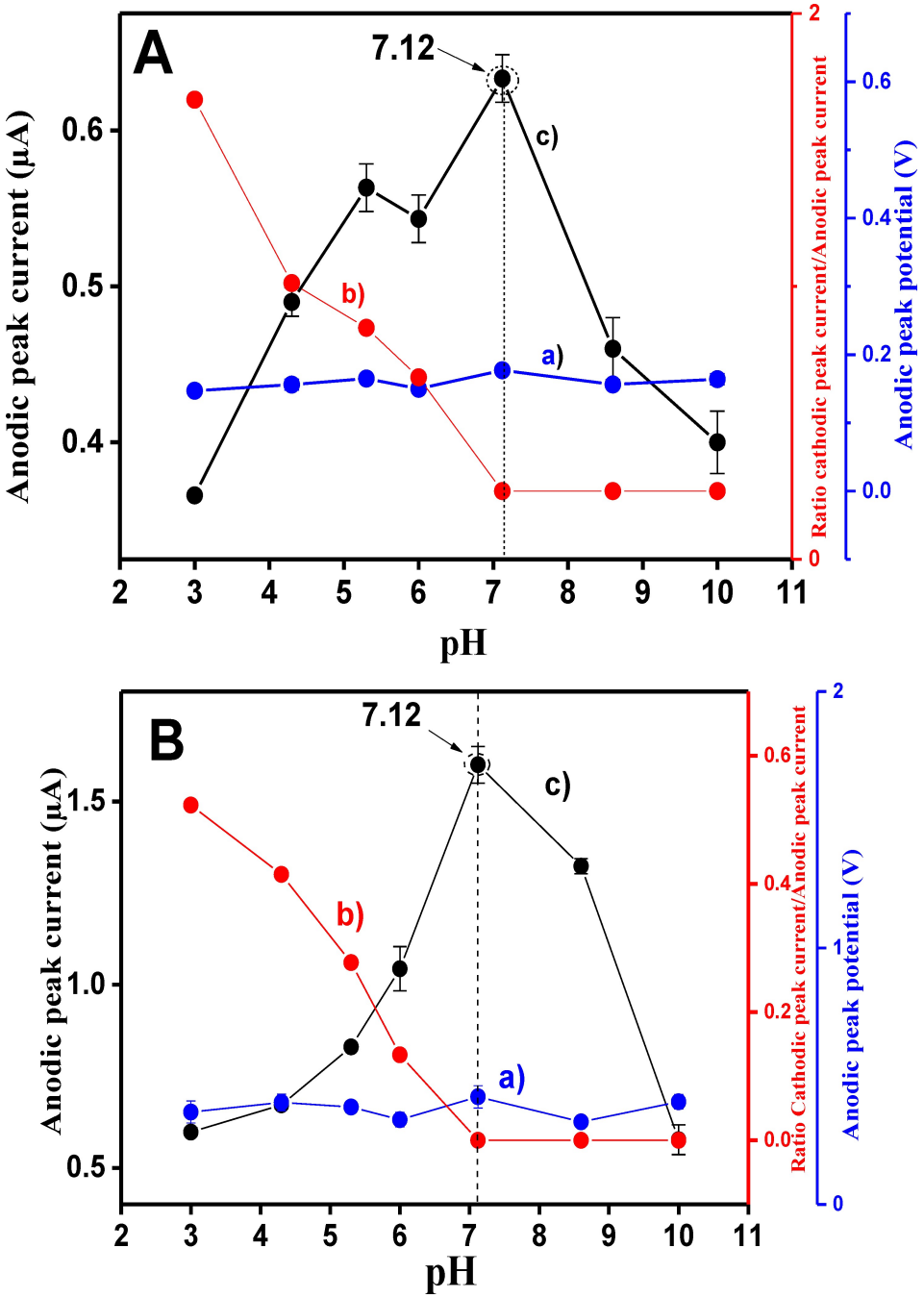

Figure 4. Plot of a) anodic peak potential, b) current ratio (Ipc/Ipa) and c) anodic peak current versus pH of the electrolyte containing 29.5 μM of CPZ recorded at **A**) SOD/GCE and **B**) SOD-GF/GCE

In neutral and basic pHs (see Figure 3B and C, respectively), at the modified electrodes, A1 changed from the reversible to an irreversible process giving a unique oxidation at CVs recorded at SOD-GF/GCE and two oxidation peaks at SOD/GCE. In both cases, no significant shift of oxidation potential of A1 was observed as pH of the buffer increases, indicating that within pH range 7–10, the oxidation process of CPZ at SOD-GF/GCE and SOD/GCE is pH independent. This result indicates that there is no proton accompanying the electron exchange during the oxidation process either in acidic or in neutral and basic pHs. Thus, at SOD/GCE and SOD-GF/GCE, the electrochemical reaction of CPZ is a simple electron transfer process[50,52] as in shown in scheme 1. The electrochemical behaviour observed at SOD/GCE can be explained by the fact that the radical ($CPZ^{+\bullet}$) formed from CPZ's oxidation through one-electron transfer process is unstable in neutral or basic solution and easily transformed to $CPZ^{2+\bullet}$ through another one-electron transfer, the latter being promptly hydrolyzed to form CPZ sulfoxide (CPZO).[50,53] Moreover, the positively charged CPZ (pKa = 9.2) may undergo a favourable electrostatic interaction with the

anionic surface of the zeolite by favouring an extrazeolite mechanism. Indeed, the size of CPZ (23.50×15.20×9.23 Å[54]) being greater than the opening of sodalite channels, is size excluded at zeolite modified electrode due to steric effect. Therefore, CPZ is more likely adsorbed or occluded on the external surface of the sodalite. Interestingly, at SOD-GF/GCE, CPZ as well as its oxidation product (CPZ) may be entrapped into large hydrophobic pores of GF containing negatively charged SOD, leading to their pre-concentration at GCE surface, which likely control the kinetics of the charge transfer process. Thanks to the good conductivity of carbon within GF, the one-step oxidation of CPZ to $CPZ^{2+\bullet}$ may occur as evidenced by increase of the oxidation peak current.

It is noteworthy that in acidic media at both modified electrodes, for the reversible process the current ratio Ip_c/Ip_a is less than unity; decreasing from 0.6 at pH 3 to 0.2 at pH 6, for SOD-GF/GCE (Figure 4B-b). The same behaviour was observed for SOD/GCE decreasing from 0.5 at pH 3 to 0.2 at pH 6 (Fig 4A-b). These results likely indicate that part of the product of the first oxidation of CPZ is reduced (C1) and another part is oxidised to give $CPZ^{2.+}$ and therefore, confirm EEC mechanism for CPZ at modified electrodes. For both modified electrodes in acid pHs, the plot of Ip versus scan rate's square root led to a straight line (inset Figure 5A and B) indicating that the current peak is under mass transport control. Meanwhile in neutral (Figure 5C and Figure 5D) and basic pHs (Figure S4), the plots of Ip_a versus *v* displayed a linear dependence, indicating that CPZ's oxidation at film GCE is an adsorption controlled process. Interestingly, at pH 7.12 the recorded CVs at SOD/GCE exhibit two one-electron irreversible peak while at SOD-GF/GCE a single irreversible CV exhibiting the highest peak current than those recorded in acidic and basic pH media. Thus, it is interesting to determine the number of electrons involved in the irreversible oxidation of CPZ at SOD-GF/GCE. Since the oxidation peak potential recorded in neutral RB pH (7.12) and basic RB (pH 10) containing 29.5 μM CPZ at SOD-GF/GCE was found to positively shift with increasing scan rate, the number of electrons transferred was estimated using Laviron theory via Eq. 3[55] and the plot of oxidative potential peak (Ep) versus log of scan rate (*v*) yields a straight line with slope of 0.049 (see Figure 5E-a for pH 7.12 and Figure 5E-b for pH 10).

By using the known charge transfer coefficient α equal to 0.5 for an irreversible process, the number of electrons involved in the CPZ's oxidation was found to be 2.35 which is ~2. This suggests that the oxidation of CPZ in neutral or basic media at SOD-GF/GCE is a one-step two-electron transfer process at pH 7.12 and pH 10.

$$E_p = E + \frac{2.303\ RT}{\alpha nF}\log\frac{RTK^{\circ}}{\alpha nF} + \frac{2.303RT}{\alpha nF}\log v \quad (3)$$

The Tafel slope b can also be estimated from Eq.4, since for totally irreversible process

$$Ep = \text{Constant} + b/2\ \log\ v \quad (4)$$

v being the scan rate. In neutral pH for instance, b = 0.049 x 2 i.e. 0.098 for the oxidation of CPZ at SOD-GF/GCE in RB pH 7.12. This value is close to the slope of Tafel plot (0.097, $R^2 = 0.999$) drawn using data from the rising part of the current voltage curve (see Figure 5F) at the scan rate 5 $mV.s^{-1}$ for 29.5 μM CPZ. This result indicates that the rate determining step for the oxidation of CPZ at the composite film GCE is a two-electron transfer with the transfer coefficient of α = 0.5 in neutral pH.

This finding suggests that the electrochemical mechanism of the oxidation of CPZ at neutral pH is likely an EC mechanism at SOD-GF/GCE (path II in scheme 1) as reported by Zhang et al[50] and Rojas et al[51] while this oxidation mechanism at SOD/GCE is an EEC mechanism (path I and III in scheme 1). As observed in Figure 6A, the peak current corresponding to the oxidation of A1 is significantly higher at SOD-GF/GCE than that recorded at SOD/GCE. This is probably because, contrary to one-electron oxidation A1 at SOD/GCE, CPZ (A1 oxidation) at SOD-GF/GCE is an one-step two-electron oxidation with a catalytic effect on oxygen evolution at A2[50] as a result of the possible π-π stacking interaction between GF and the aromatic group of CPZ.[56]

Electroanalysis of CPZ at SOD/GCE and SOD-GF/GCE

The quantification of CPZ in aqueous media was achieved using differential pulse voltammetry (DPV) technique and Figure 6B presents the DPV recorded in potential window +0.1–+1 V at unmodified GCE (curve a) and GCE overcoated with a film of either SOD/GCE (curve b) or SOD-GF/GCE (curve c). It can be observed that at bare and modified GCE, DPVs exhibits well-defined oxidation peak located at +0.65 V corresponding to the A1 oxidation as discussed in the section above. Interestingly, the oxidation peak current obtained at SOD-GF/GCE was 6-fold that obtained at bare GCE and 3-fold that of SOD-GCE (i.e., $Ip\text{-}_{GCE} = 1.10 \pm 0.10$ μA; $Ip\text{-}_{SOD\text{-}GCE} = 2.30 \pm 0.12$ μA and $Ip\text{-}_{SOD\text{-}GF/GCE} = 6.25 \pm 0.05$ μA) in accordance with oxidation response recorded using cyclic voltammetry. These results indicate that the modified electrodes are sensitive toward CPZ and thus can be applied in the quantification of this compound.

Optimal Electroanalysis Conditions

Prior to the utilization of the modified electrodes for the electroanalysis of CPZ, the optimal conditions for its determination have been defined including effect of SOD-GF composition, pH of the electrolyte and accumulation time.

The effect of SOD-GF composition on the DPV electrochemical response of CPZ was studied by varying the amount of GF in the composite. Figure S5 shows the plot of oxidation peak current versus the weight percentage of GF in the composite. It can be observed that the increase of GF content from 0% in the composite led to the gradual increase of the CPZ oxidation signal with a maximum at 10% GF and then levelled off. In fact, of the augmentation of GF's amount led to the increase of electronic conductivity of the modified electrode

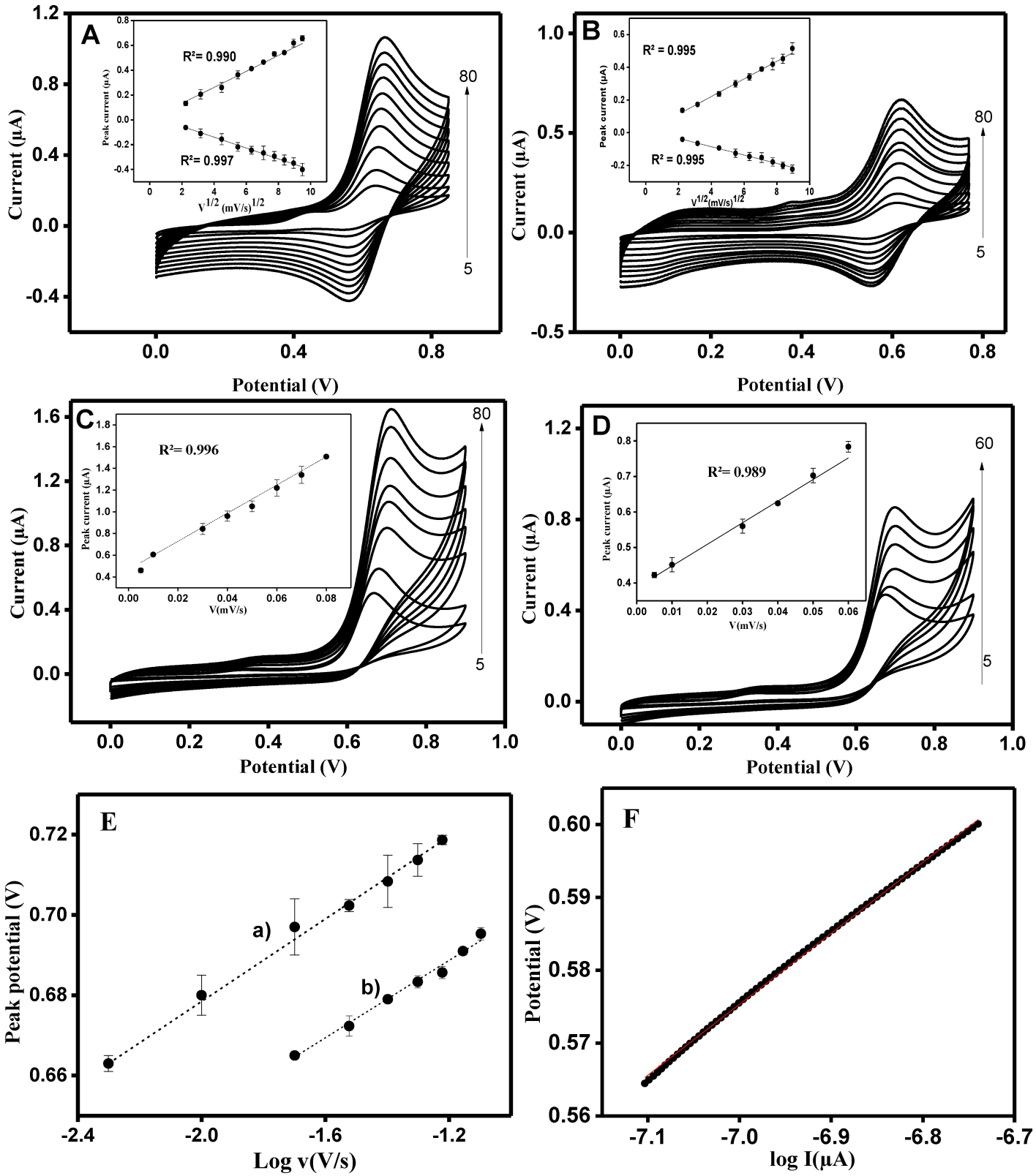

Figure 5. Cyclic voltammograms recorded at different scan rates containing 29.5 μM of CPZ for A), B) RB pH 3 and C), D) RB (pH 7.12); Inset of Plot of oxidation peak current versus $v^{1/2}$ at pH 3 and current versus scan rates at pH 7.12. E) plot of oxidation peak potential versus log V recorded in a) RB pH 7.12 and b) RB pH 10. F) Tafel plots for SOD-GF/GCE at a scan rate of 5 mV/s in RB pH 7.12 containing 29.5 μM of CPZ.

via the π-π interaction between the phenyl structure of CPZ and the GF favouring its oxidation via one-step two-electron process. Higher GF quantity in the composite (above 10%) led to a poor signature of CPZ likely because of the hydrophobicity

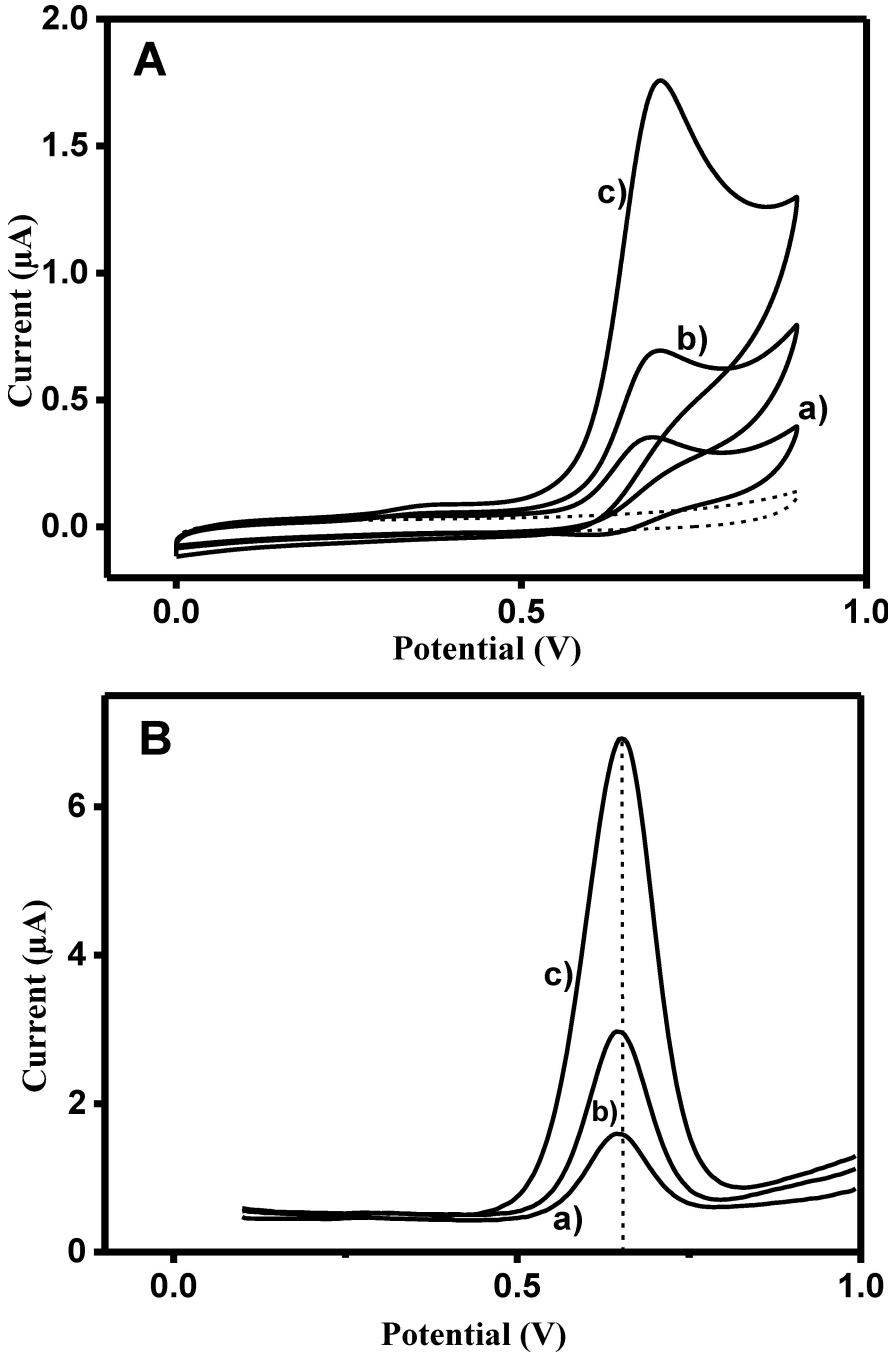

Figure 6. A) CVs recorded at 50 mV/s and **B**) DPVs. Voltammograms recorded in RB (pH 7.12) containing 29.5 μM CPZ at (a) bare GCE, (b) SOD/GCE and (c) SOD-GF/GCE.

character of GF[57] and thus less stability of the film onto GCE surface.

Figure S6 shows CVs recorded in RB solution containing 29.5 μM of CPZ at different pH values ranging from 3–10. Figure 4A and B (CV c)) shows the plot of A1 oxidation current peak versus electrolyte pH for SOD/GCE and SOD-GF/GCE respectively. It is worth noting that the current due to CPZ oxidation augments with increasing pH from 3 to 7.12 then decreases above; thus 7.12 was retained as optimal pH for both modified electrodes.

As demonstrated earlier in the section above, the electrooxidation of CPZ at SOD/GF/GCE is controlled by the adsorption, thus the effect of the accumulation time on the electrochemical response was studied. It is worth noting that the increasing accumulation time led to the gradual increase of oxidation peak current until it reaches the maximum for 3.6 min and then decreases above this time (see Figure S7). Thus, 3.6 min was retained as pre-concentration time for all experimental analyses.

Calibration, Selectivity and Interferences

The performance of SOD/GCE and SOD-GF/GCE were studied at various concentrations under optimal conditions (RB pH 7.12 and accumulation time 3.6 min) using DPV technique. Figure 7A displays the DPVs recorded for various concentrations at SOD-GF/GCE and SOD/GCE (inset Figure 7A) where it is clearly observed, the increase of current peak with consecutive added concentration of CPZ from 0.5 μM to 29.5 μM for both electrodes. The calibration plots show that at both modified electrodes, the oxidation current and concentration are linearly dependent with regression equation Ipa = (0.080 ± 0.001) [CPZ] – (0.005 ± 0.004) (R^2 = 0.994) and Ipa = 0.220 ± 0.003 [CPZ] – 0.037 ± 0.011 (R^2 = 0.993) for SOD/GCE (Fig 7B-a) and SOD-GF/GCE (Fig 7B-b) respectively. The detection limits for SOD and SOD-GF/GCE were also estimated and were found to be 0.090 ± 0.001 μM and 0.020 ± 0.002 μM, respectively. Table 2 below compares the analytical performance of the prepared sensor with those reported in the literature. It can be observed that the prepared sensors exhibit appreciable linear range concentration with lower detection limit compared to most of the previously reported sensors.

The selectivity of the developed sensor was studied by evaluating the effect of potential interfering molecules (uric and ascorbic acid, glucose and acetaminophen) on the electroanalysis of CPZ under the same experimental conditions as described above. As shown in Figure S8, it was found that the electrochemical response of CPZ (7 μM) remained constant while adding acetaminophen up to ca 8 times higher than CPZ, indicating that acetaminophen did not interfere with the detection of CPZ, meanwhile the addition of uric and ascorbic acid (≥ 10 μM) interfered with the CPZ oxidation as highlighted by the increase of the electrochemical oxidation response of CPZ.

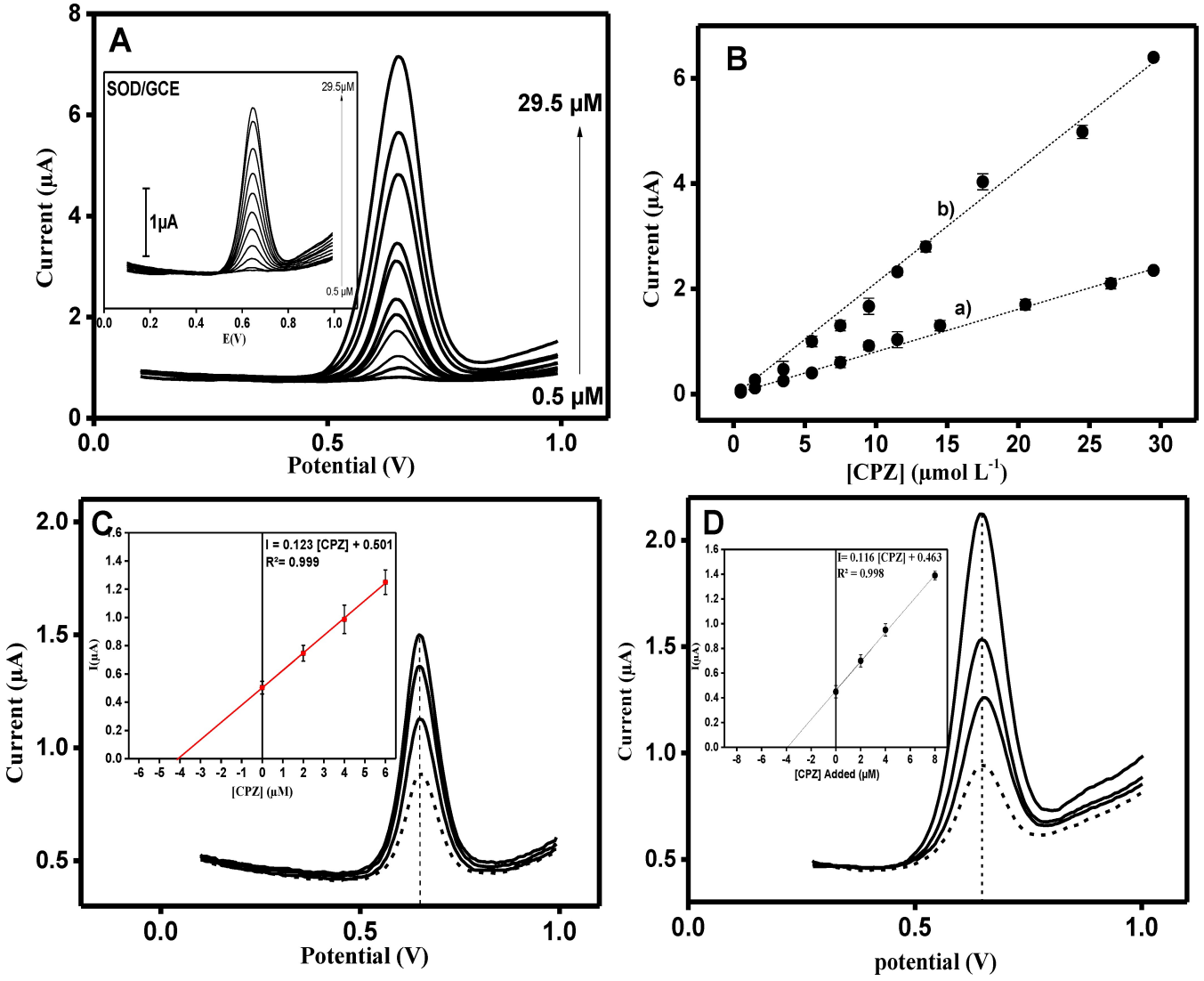

Figure 7. DPVs recorded in RB (pH 7.12) at **A)** SOD-GF/GCE with successive addition of CPZ. The insets show DPVs recorded in at SOD/GCE in the same conditions at SOD-GF/GCE. **B**) Plot of the corresponding oxidation peak current versus the concentration of CPZ at **a**) SOD/GCE and **b**) SOD-GF/GCE. DPVs recorded in RB pH 7.12 containing real sample (dashed line) at SOD-GF/GCE with successive addition of CPZ standard for **C)** tablet and **D)** tap water. The insets show the corresponding calibration curve.

Table 2. Comparison of analytical performances of SOD/GCE and SOD-GF/GCE with those of sensors reported in the literature for CPZ electroanalysis.

Sensors	Technique	Concentration range (μM)	LOD (μM)	References
GO-Fe/ZnO/SPCE	DPV	0.02–172.74	0.02	[28]
BDDE	DPV	0.1–40	3	[58]
MWCNT-PEI/GCE	DPV	0.019–9.2	0.01	[59]
L-Cys-CPE	DPV	1–35	0.0119	[60]
P3MT/γ -CD/GCE	SWV	0.14–3.363	0.1	[27a]
Bi/PSi/MWCNT/CPE	DPV	0.1–260	17	[61]
$ZnMnO_3$/ZnO NPs/GCE	DPV	0.05–125.55	0.019	[62]
SOD/GCE	DPV	0.5-29.5	0.09	This work
SOD-GF/GCE			0.02	

GO-Fe/ZnO/SPCE : iron nanoparticles-loaded graphene oxide/three dimensional honeycomb-like zinc oxide (ZnO) nanohybrid modified screen printed carbon electrode ; BDDE : boron-doped diamond electrode ; MWCNT-PEI/GCE : multiwalled carbon nanotube-polyethyleneimine composite modified glassy carbon electrode ; L-Cys-CPE: L-Cysteine modified carbon paste electrode ; P3MT/γ -CD/GCE : Poly-3-methylthiophene combined with γ-cyclodextrin modified glassy carbon electrode ; Bi/PSi/MWCNT/CPE : bismuth/porous silicon/multiwalled carbon nanotube modified carbon paste electrode ; $ZnMnO_3$/ZnO NPs/GCE : heterostructure of mixed metal oxide cubic zinc-manganaese oxide ($ZnMnO_3$) and hexagonal zinc oxide Nanoparticles.

Reproducibility, Repeatability and Long-Term Stability

The reproducibility of SOD-GF/GCE was assessed by performing six replicates detection of 20 μM CPZ in RB pH 7.12 using six independent electrodes prepared in the same conditions as described in the caption of Figure 7. The recorded DPVs are presented in Figure S9 A. The data collected from these DPVs show that the developed sensors exhibited good reproducibility with percentage relative standard deviation of 6.08 %. Furthermore, the repeatability was studied by performing six consecutive measurements as shown in Figure S9 B, which revealed that the SOD-GF/GCE retained about 95.6 % of the initial current due to CPZ's oxidation. The stability of the prepared sensors was also evaluated for one month by measuring current response of 18 μM of CPZ contained in RB using DPV. After each measurement and desorption, the sensors were rinsed with distilled water and kept dried at room temperature. The data recorded (Figure S9 C) show that the sensors retained 91 % of the initial current. All the results mentioned above demonstrate the developed sensors are promising candidate for the electroanalysis of CPZ with good stability and reproducibility.

Quantification of CPZ in Real Sample

The modified electrode SOD-GF/GCE was applied to quantify CPZ in a pharmaceutical tablet and in tap water using standard addition method. To achieve this, CPZ tablet and CPZ water samples were prepared as described in the experimental section. As shown in Figure 7, when the diluted tablet (Figure 7C) or CPZ from tap water (Fig 7D) was added in the electrolyte solution (RB pH = 7.12), well resolved oxidation peaks were recorded (dashed line) at modified electrode SOD-GF/GCE. The addition of the standard in the former electrolyte solution containing CPZ (real sample), led to the increase of CPZ oxidation peaks while increasing the amount of standard (solid lines). The plot of the added concentration of standard versus the electrochemical response indicate a linear dependence between Ipa and concentration of the CPZ standard. The exploitation of these different straight lines helps to determine the concentration of the added real samples. The results summarized in table 3 show that the percentage of CPZ recovery in the drug tablet and in tap water ranged from 95 to 101 %. These results show the accuracy and the precision of the developed methods, which further will validate the application of the developed sensors for the determination of CPZ in a complex matrix.

Conclusion

This work reported the synthesis of nanosodalite from beneficiated kaolin using solid-solid transformation without organic template and the utilization of the as-synthesised material in the preparation of sodalite-graphene foam composite. The physico-chemical characterization of the zeolite reveals a pure crystalline sodalite with 38.3 nm crystallite size and 22 m^2/g surface area. Meanwhile, the nanocomposite exhibits a larger surface area, four times that of pristine sodalite, attributed to the presence of porous GF. The results of the structural and morphological analyses reveal a well-correlated composite in which the crystalline structure of each material is preserved. The obtained composite was subsequently used to prepare sensors by coating a film on glassy carbon electrode.

The electrochemical characterization of the composite reveals that the presence of GF increases the charge transfer capability of the sensor compared to SOD/GCE, thus demonstrating that nanosodalite as well as graphene-sodalite composite could be a promising material for modified electrodes. The modified electrodes were used to study the electrochemistry of CPZ aqueous media and it was observed that the electrochemical behaviour of CPZ depends on both the electrolyte pH and the nature of the electrodes. From this study, it was found

Table 3. Qquantification of CPZ in a drug tablet and in a tap water

Real Samples	Added (μM)	Found (μM)	RSD (%)
Largactil	2	1.90 ± 0.01	95.45 ± 0.52
	4	4.02 ± 0.15	100.65 ± 3.73
	6	5.74 ± 0.05	95.66 ± 0.90
Tap water	2	1.92 ± 0.06	96.15 ± 3.12
	4	3.99 ± 0.03	99.77 ± 0.65

that the electrochemical mechanism of the target analyte at the composite modified electrodes is either an Electrochemical-Electrochemical and Chemistry (EEC) mechanism or Electrochemical and Chemistry (EC) mechanism depending on the pH range while this mechanism is an EEC mechanism at SOD/GCE over the pH range studied. Both modified electrodes were used to sense chlorpromazine in aqueous media, SOD-GF/GCE exhibiting the highest sensibility due to the high surface area GF as well as the favorable π-π stacking interaction between graphene and of the aromatic group of CPZ. Under optimal experimental conditions, the composite film modified GCE was used successfully in CPZ's electroanalysis in aqueous solution within a large concentration range with low detection limit (0.09 μM for SOD/GCE and 0.02 μM for SOD-GF/GCE). The composite based sensors were also successfully used to quantify CPZ in tablet and tap water with appreciable percentage recovery ranging from 95–101 %.

Acknowledgements

The financial support from Royal Society UK and UK aid (ROYAL SOCIETY-FCDO, Grant N° AQ 150029-ACBI program) is acknowledged gratefully. HWL gratefully acknowledged the South African Research Chairs Initiative (SARChI) of the Department of Science and Innovation, and the National Research Foundation (Grant N° 150526)

Conflict of Interests

There is no conflict to declare.

Data Availability Statement

The data that support the findings of this study are available in the supplementary material of this article.

Keywords: Kaolin · nanosodalite · graphene foam · composite · modified electrode · chlorpromazine

[1] W. Kutner, J. Wang, M. L'her, R. P. Buck, *Pure Appl. Chem.* **1998**, *70*, 1301–1318.
[2] J. C. Kemmegne-Mbouguen, E. Ngameni, P. G. Baker, T. T. Waryo, B. Kgarebe, E. I. Iwuoha, *Int. J. Electrochem. Sci.* **2014**, *9*, 478–492.
[3] a) M. C. Ngo Ngwem, J. C. Kemmegne-Mbouguen, H. W. Langmi, N. M. Musyoka, R. Mokaya, *ChemistrySelect* **2022**, *7*, e202202308; b) E. Mouafo-Tchinda, J. C. Kemmegne-Mbouguen, C. P. Nanseu-Njiki, H. W. Langmi, C. Kowenje, N. M. Musyoka, R. Mokaya, *RSC Adv.* **2023**, *13*, 20816–20829.
[4] F. Parfait Tchoumi, A. Kamdem Tamo, G. Doungmo, C. G. Fotsop, J. Kemmegne-Mbouguen, *J. Appl. Electrochem.* **2023**, 1–18.
[5] C. Rios, C. Williams, O. Castellanos, *Mater. Res.* **2013**, *16*, 424–438.
[6] A. Mikuła, M. Król, A. Koleżyński, *J. Mol. Struct.* **2016**, *1126*, 110–116.
[7] J. Yao, L. Zhang, H. Wang, *Mater. Lett.* **2008**, *62*, 4028–4030.
[8] a) M. S. Nabavi, T. Mohammadi, M. Kazemimoghadam, *Ceram. Int.* **2014**, *40*, 5889–5896; b) S. Goel, Z. Wu, S. I. Zones, E. Iglesia, *J. Am. Chem. Soc.* **2012**, *134*, 17688–17695; c) G. Yang, H. Guo, Z. Kang, L. Zhao, S. Feng, F. Jiao, S. Mintova, *ChemSusChem* **2019**, *12*, 4529–4537.
[9] A. W. C. van den Berg, S. T. Bromley, J. C. Jansen, *Microporous Mesoporous Mater.* **2005**, *78*, 63–71.
[10] a) N. Jantarit, P. Tayraukham, N. Osakoo, K. Föttinger, J. Wittayakun, *Mater. Res. Express* **2020**, *7*, 075011; b) N. Hiyoshi, *Appl. Catal. A* **2012**, *419*, 164–169.
[11] G. V. Shanbhag, M. Choi, J. Kim, R. Ryoo, *J. Catal.* **2009**, *264*, 88–92.
[12] K. L. T. Nguena, C. G. Fotsop, S. B. L. Ngomade, A. K. Tamo, C. A. Madu, F. Ezema, E. E. Oguzie, *Mater. Today Commun.* **2023**, *37*, 107406.
[13] J. Li, X. Zeng, X. Yang, C. Wang, X. Luo, *Mater. Lett.* **2015**, *161*, 157–159.
[14] a) S.-R. Lee, M. Park, Y.-S. Han, J.-H. Choy, *J. Phys. Chem. Solids* **2004**, *65*, 421–424; b) M. Xiao, X. Hu, Y. Gong, D. Gao, P. Zhang, Q. Liu, Y. Liu, M. Wang, *RSC Adv.* **2015**, *5*, 100743–100749.
[15] A. Walcarius, T. Barbaise, J. Bessiere, *Anal. Chim. Acta* **1997**, *340*, 61–76.
[16] B. Kaur, R. Srivastava, *Electroanalysis* **2014**, *26*, 1739–1750.
[17] M. Rahimnejad, S. K. Hassaninejad-Darzi, S. M. Pourali, *J. Iran. Chem. Soc.* **2015**, *12*, 413–425.
[18] a) P. Wei, Z. Li, Y. E, Y. Jiang, P. Chen, L. Li, T. F. Krenzel, K. Qian, *Mater. Res. Bull.* **2024**, *170*, 112564; b) P. Wei, Z. Li, Y. E, Y. Jiang, P. Chen, L. Li, T. F. Krenzel, K. Qian, *Biosens. Bioelectron.* **2023**, *239*, 115631.
[19] a) N. S. Hudepohl, H. A. Nasrallah, *Handb. Clin. Neurol.* **2012**, *106*, 657–667; b) J. Jankowska-Śliwińska, M. Dawgul, D. G. Pijanowska, *Procedia Eng.* **2014**, *87*, 747–750.
[20] B. K. Lester, J. D. Coulter, L. C. Cowden, H. L. Williams, *Psychopharmacologia* **1971**, *20*, 280–287.
[21] P. Biswas, B. P. Vellanki, A. A. Kazmi, *Sci. Total Environ.* **2022**, *824*, 153757.
[22] K. Murakami, K. Murakami, T. Ueno, J. Hijikata, K. Shirasawa, T. Muto, *J. Chromatogr. B* **1982**, *227*, 103–112.
[23] C. S. de la Torre, M. A. Martínez, E. Almarza, *Forensic Sci. Int.* **2005**, *155*, 193–204.
[24] J. M. Calatayud, C. G. Benito, *Anal. Chim. Acta* **1992**, *256*, 105–111.
[25] a) Y. Kohl, N. William, E. Elje, N. Backes, M. Rothbauer, A. Srancikova, E. Rundén-Pran, N. El Yamani, R. Korenstein, L. Madi, A. Barbul, K. Kozics, M. Sramkova, K. Steenson, A. Gabelova, P. Ertl, M. Dusinska, A. Nelson, *Bioelectrochemistry* **2023**, *153*, 108467; b) J. Owen, M. Kuznecovs, R. Bhamji, N. William, N. Domenech-Garcia, M. Hesler, T. Knoll, Y. Kohl, A. Nelson, N. Kapur, *Rev. Sci. Instrum.* **2020**, *91*.
[26] S. Mohamadi, D. J. Tate, A. Vakurov, A. Nelson, *Anal. Chim. Acta* **2014**, *813*, 83–89.
[27] a) D. Bouchta, N. Izaoumen, H. Zejli, M. El Kaoutit, K. R. Temsamani, *Biosens. Bioelectron.* **2005**, *20*, 2228–2235; b) V. Vinothkumar, G. Kesavan, S.-M. Chen, *J. Electroanal. Chem.* **2021**, *895*, 115535; c) V. Vinothkumar, R. Sakthivel, S.-M. Chen, M. Abinaya, S. Kubendhiran, *J. Alloys Compd.* **2021**, *888*, 161537.
[28] N. Sebastian, W.-C. Yu, Y.-C. Hu, D. Balram, Y.-H. Yu, *Ultrason. Sonochem.* **2019**, *59*, 104696.
[29] J. C. Kemmegne-Mbouguen, F. P. Tchoumi, *J. Solid State Electrochem.* **2023**, *27*, 939–953.
[30] S. E. Bambalaza, H. W. Langmi, N. M. Musyoka, J. Ren, L. E. Khotseng, *Mater. Today: Proc.* **2018**, *5*, 10431–10439.
[31] J. H. Choy, S.-R. Lee, Y.-S. Han, M. Park, G.-S. Park, *Chem. Commun.* **2003**, 1922–1923.
[32] M. M. Treacy, J. B. Higgins, *Collection of simulated XRD powder patterns for zeolites fifth (5th) revised edition*, Elsevier, **2007**.
[33] Q. Song, J. Shen, Y. Yang, J. Wang, Y. Yang, J. Sun, B. Jiang, Z. Liao, *Microporous Mesoporous Mater.* **2020**, *292*, 109755.
[34] F. Navarro-Pardo, G. Martínez-Barrera, A. L. Martínez-Hernández, V. M. Castaño, J. L. Rivera-Armenta, F. Medellín-Rodríguez, C. Velasco-Santos, *Materials* **2013**, *6*, 3494–3513.
[35] E. M. Flanigen, H. Khatami, H. A. Szymanski, in *Molecular Sieve Zeolites-I, Vol. 101*, AMERICAN CHEMICAL SOCIETY, **1974**, pp. 201–229.
[36] M. Alkan, Ç. Hopa, Z. Yilmaz, H. Güler, *Microporous Mesoporous Mater.* **2005**, *86*, 176–184.
[37] A. Demortier, N. Gobeltz, J. P. Lelieur, C. Duhayon, *Int. J. Inorg. Mater.* **1999**, *1*, 129–134.
[38] S.-R. Lee, Y.-S. Han, J.-H. Choy, *Solid State Ionics* **2002**, *151*, 343–346.
[39] I. O. Ali, S. M. El-Sheikh, T. M. Salama, E. Abdel-Khalek, M. Thabet, M. F. Bakr, M. H. Fodial, *J. Inorg. Organomet. Polym. Mater.* **2021**, *31*, 577–590.
[40] M. Khatamian, B. Divband, F. Farahmand-zahed, *Mater. Sci. Eng. C* **2016**, *66*, 251–258.
[41] a) R. Askarnia, B. Ghasemi, S. R. Fardi, E. Adabifiroozjaei, *Surf. Coat. Technol.* **2020**, *403*, 126410; b) D. P. Narayanan, A. Gopalakrishnan, Z. Yaakob, S. Sugunan, B. N. Narayanan, *Arab. J. Chem.* **2020**, *13*, 318–334; c) C. K. Choi, *J. Korean Phys. Soc.* **2010**, *56*, 1150–1155.

[42] E. Enríquez, J. F. Fernández, M. A. de la Rubia, *Carbon* **2012**, *50*, 4409–4417.
[43] M. Esaifan, L. N. Warr, G. Grathoff, T. Meyer, M.-T. Schafmeister, A. Kruth, H. Testrich, *Minerals* **2019**, *9*, 484.
[44] a) F. A. C. M. Passos, D. C. Castro, K. K. Ferreira, K. M. A. Simões, L. C. Bertolino, C. N. Barbato, F. M. S. Garrido, A. A. S. Felix, F. A. N. G. Silva, in *Characterization of Minerals, Metals, and Materials 2017* (Eds.: S. Ikhmayies, B. Li, J. S. Carpenter, J. Li, J.-Y. Hwang, S. N. Monteiro, D. Firrao, M. Zhang, Z. Peng, J. P. Escobedo-Diaz, C. Bai, Y. E. Kalay, R. Goswami, J. Kim), Springer International Publishing, Cham, **2017**, pp. 279–288; b) B. Makgabutlane, L. N. Nthunya, N. Musyoka, B. S. Dladla, E. N. Nxumalo, S. D. Mhlanga, *RSC Adv.* **2020**, *10*, 2416–2427.
[45] T. Kuzniatsova, Y. Kim, K. Shqau, P. K. Dutta, H. Verweij, *Microporous Mesoporous Mater.* **2007**, *103*, 102–107.
[46] J. S. Sohn, U. M. Patil, S. Kang, S. Kang, S. C. Jun, *RSC Adv.* **2015**, *5*, 107864–107871.
[47] N. M. Musyoka, L. F. Petrik, E. Hums, A. Kuhnt, W. Schwieger, *Res. Chem. Intermed.* **2015**, *41*, 575–582.
[48] T. Shah, K. Dad, S. Akbar, R. Shahnaz, *J. Chem. Soc. Pak.* **2011**, *27*, 456.
[49] S. Khajavi, S. Sartipi, J. Gascon, J. Jansen, F. Kapteijn, *Microporous Mesoporous Mater.* **2010**, *132*, 510–517.
[50] M. Zhang, W.-Q. Bao, Y. Wang, N. Deng, J.-B. He, *J. Electroanal. Chem.* **2014**, *724*, 1–7.
[51] F. Martinez-Rojas, C. Espinosa-Bustos, G. Ramirez, F. Armijo, *Electrochim. Acta* **2023**, *443*, 141873.
[52] G. Kesavan, P. K. Gopi, S.-M. Chen, V. Vinothkumar, *J. Electroanal. Chem.* **2021**, *882*, 114982.
[53] V. N. Palakollu, R. Karpoormath, L. Wang, J.-N. Tang, C. Liu, *Nanomaterials* **2020**, *10*, 1513.
[54] J. McDowell, *Acta Crystallogr. Sect. B* **1969**, *25*, 2175–2181.
[55] E. Laviron, *J. Electroanal. Chem. Interfacial Electrochem.* **1979**, *101*, 19–28.
[56] a) A. Karton, *Chem. Phys.* **2022**, *561*, 111606; b) S. Lakard, I.-A. Pavel, B. Lakard, *Biosensors* **2021**, *11*, 179.
[57] L. C. Figueiredo-Filho, D. A. Brownson, O. Fatibello-Filho, C. E. Banks, *Electroanalysis* **2014**, *26*, 93–102.
[58] B. B. Petković, D. Kuzmanović, T. Dimitrijević, M. P. Krstić, D. M. Stanković, *Int. J. Electrochem. Sci.* **2017**, *12*, 3709–3720.
[59] B. Unnikrishnan, P.-C. Hsu, S.-M. Chen, *Int. J. Electrochem. Sci.* **2012**, *7*, 11414–11425.
[60] H. Purushothama, Y. A. Nayaka, P. Manjunatha, R. Yathisha, M. Vinay, K. Basavarajappa, *Chem. Data Collect.* **2019**, *23*, 100268.
[61] A. Ensafi, P. Hedayati, M. M. Abarghoui, B. Rezaei, *Electroanalysis* **2017**, *29*, 2461–2469.
[62] K. Balamurugan, R. Karthik, S.-M. Chen, R. Sukanya, B. Thasma Subramanian, V. M. N. Biju, J.-J. Shim, C. B. Breslin, *Composites Part B* **2022**, *236*, 109822.

Manuscript received: January 26, 2024
Revised manuscript received: May 8, 2024
Version of record online: June 19, 2024